Phase diagram of the charged lattice-gas model with two types of particles

G. Lehaut, F. Gulminelli, and O. Lopez
LPC Caen, ENSICAEN, Université de Caen–CNRS/IN2P3, Caen, France
(Received 25 September 2009; published 6 May 2010)

A lattice-gas model with two types of particles, a particle-dependent short-range coupling and a long-range repulsive Coulombic interaction, is introduced. The phase diagram of an isolated finite system of 129 particles is constructed using the bimodality properties of the observables' distribution. We show that this generic Hamiltonian, with couplings optimized on the properties of the atomic nucleus, exhibits a specific phase diagram including, together with the well-known liquid-gas phase transition, a segregation phase that can be assimilated to nuclear fission.

DOI: 10.1103/PhysRevE.81.051104 PACS number(s): 05.50.+q, 68.35.Rh, 24.10.Pa

I. INTRODUCTION

Lattice-gas models are well-known useful tools to explore the generic properties of interacting systems belonging to different universality classes [1]. In such models, different couplings and frustrating interactions can be used to study the basic features of the phase diagram of a large body of systems. Examples are binary fluids [2], metallic alloys [3], adatoms on a crystal surface [4], ^{3}He-^{4}He mixtures [5], nuclear matter [6], magnetic films [7], glass-forming liquids [8], polymer mixtures [9], or neutron star crusts [10]. These models are indeed particularly adapted to study the thermodynamics of finite systems and the effect of the different constraints or statistical ensembles [11–15].

Concerning the specific example of atomic nuclei, lattice-gas models have been employed since more than one decade [16–18] and even quantitatively compared to experimental data of nuclear structure and nuclear fragmentation [18–21]. If cluster observables have been computed by many authors, thermodynamic studies of these systems are however scarce [12,13,17,22] and never consider on a same footing the fact that both the short-range ferromagnetic interaction and the long-range Coulombic interaction should be isospin dependent, i.e., different for protons and neutrons.

In this paper we consider an isolated finite lattice-gas system composed of two types of particles (charged and neutral particles) with a schematic Hamiltonian including both the Coulomb field and the symmetry energy, which are short- and long-range couplings depending on the particle type. After a short presentation of the model in Sec. II, the ground-state properties of this system are studied in Sec. III with a simulated annealing technique. As a function of the number of charged particles Z and number of neutral particles N, we observe instability lines associated with phenomena qualitatively similar to the well-known nuclear phenomena of nucleon emission at drip lines and spontaneous fission.

The finite-temperature phase diagram of the model is then studied in Sec. IV with a Metropolis technique. A first-order liquid-gas phase transition line is observed. Together with this transition, already known from the simpler uncharged version of the model containing only one type of particles, an extra transition is observed to a fragmentation phase which is specific to the frustrating isospin-dependent interaction. Possible connections to other physical systems and experimental observations are developed in the Conclusion section. Some of the results presented in this paper have been already published in Ref. [23].

II. MODEL

We consider a system composed of N neutral and Z charged particles of mass m occupying a cubic lattice of $L^3=8000$ cells with four degrees of freedom: one discrete variable σ_i for isospin ($\sigma_i=1$ for charged particles, $\sigma_i=-1$ for neutral particles, and $\sigma_i=0$ if the site is unoccupied) and three continuous variables $\vec{p_i}$ for the momentum. The Hamiltonian is given by

$$H = H_{nuc} + H_{coul} + H_{kin} \tag{1}$$

$$= \sum_{\langle i,j\rangle} \epsilon_{\sigma_i\sigma_j}\sigma_i\sigma_j + \sum_{\sigma_i=\sigma_j=1, i\neq j} \frac{I_c}{r_{ij}} + \sum_{i=1}^{L^3} \frac{p_i^2}{2m}\sigma_i^2, \tag{2}$$

where $\langle i,j\rangle$ are nearest-neighbor cells, $\epsilon_{\sigma_i\sigma_j}$ is their coupling, I_c is the Coulomb coupling, and r_{ij} is the distance between sites i and j. The standard version of this model [16,17], which we will denote by H_{scalar} and calculate in the following for comparison with the full Hamiltonian H, assumes uniquely a constant short-range ferromagnetic coupling: $\epsilon_{11}=\epsilon_{-1-1}=\epsilon_{1-1}=\epsilon>0$, $I_c=0$.

To include Coulomb and symmetry energy effects as in the nuclear physics case one has to take $\epsilon_{11}=\epsilon_{-1-1}\leq 0$, $\epsilon_{1-1}>0$, $I_c>0$ [18,24]. A lattice spacing $r_0=1.8$ fm results in a density for an infinite system at full lattice occupation $r_0^{-3}=\rho_0=0.17$ fm^{-3}, corresponding to the saturation density of symmetric nuclear matter. The choice of $I_c=1.44$ MeV fm, $m=939$ MeV, $\epsilon_{-1,1}\equiv\epsilon=5.5$ MeV, $\epsilon_{-1-1}=0$ further provides the correct saturation and symmetry energy of nuclear matter [24] at full occupation.

In the following, we will note E_{nuc} as the energy contribution of the short-range interaction,

$$E_{nuc} = \left\langle \sum_{\langle i,j\rangle} \epsilon_{\sigma_i\sigma_j}\sigma_i\sigma_j \right\rangle, \tag{3}$$

E_{kin} the kinetic energy,

$$E_{kin} = \left\langle \sum_{i=1}^{L^3} \frac{p_i^2}{2m} \sigma_i^2 \right\rangle, \tag{4}$$

and E_{coul} will give the long-range Coulombic energy,

$$E_{coul} = \left\langle \sum_{\sigma_i=\sigma_j=1, i\neq j} \frac{I_c}{r_{ij}} \right\rangle, \tag{5}$$

where $\langle \cdot \rangle$ indicates thermal averages. We will also note the total potential energy $E_{int}=E_{nuc}+E_{coul}$ and the total energy $E_{tot}=E_{nuc}+E_{coul}+E_{kin}$.

Ensembles of occupied sites constitute clusters. These latter are defined according to the following rule known in the literature as the Hill's cluster definition [25]. Two occupied sites ("nucleons") (i,j) belong to the same cluster if they are close neighbors and they additionally fulfill

$$E_{rel} < |\epsilon_{\sigma_i\sigma_j}|, \tag{6}$$

with

$$E_{rel} = \frac{\mu}{2} v_{rel}^2,$$

where $\mu=m/2$ is the reduced mass and $v_{rel}=|\vec{p}_i-\vec{p}_j|/m$ is the relative velocity of the two nucleons.

Definition (6) represents only a local criterion in contrast to more sophisticated global cluster definitions which have been proposed in the literature as the early cluster recognition algorithm (ECRA) definition [26]. It was shown [25] that clusters defined according to the above rule in average are self-bound; this means that, if one would consider a dynamical evolution of the system under the action of the Hamiltonian (2), the cluster size distribution would not be modified in average as a function of time. This means that Coniglio-Klein clusters are physical clusters that can be, at least qualitatively, compared to experimental data.

This lattice-gas model was already shown to give a qualitative description of nuclear fragmentation [18]. Moreover, its simplified version H_{scalar} with uncharged particles is isomorphous to a generic model in statistical mechanics, the spin-1 Ising model [5], which makes the lattice-gas model (LGM) a paradigm of phase transitions in finite systems. The universal character of phase transitions implies that observables expressed in reduced adimensional units are expected to be similar within systems belonging to the same universality class as Coulombic binary fluids, spin-1 lattices, or atomic nuclei.

Calculations are made in the isobar ensemble, which is the optimal canonical ensemble to describe unbound systems in the vacuum [27]. The canonical partition function of the isobar ensemble reads

$$\Omega = \sum_{(n)} \exp[-\beta(H^{(n)} + PV^{(n)})], \tag{7}$$

where β, P are Lagrange parameters, the sum runs over all the possible realizations (n), $H^{(n)}$ is the total energy for each partition (n), and $V^{(n)}$ is the global extension of the system defined as

$$V^{(n)} = 2\left(\sum r_i^3 \sigma_i^2\right)^{(n)} \Big/ \left(\sum \sigma_i^2\right)^{(n)}, \tag{8}$$

where r_i is the distance between site i and the center of the lattice. The statistical average $\langle V^{(n)} \rangle$ at a given value of T and P will be denoted by R^3 in the following [28].

Isolated systems in the vacuum as atomic nuclei are best described by the microcanonical ensemble [13,29,30]. To extract the microcanonical distribution it is useful to recall the relationship between the canonical probability distribution and the microcanonical isobaric entropy in finite systems,

$$p_{\beta,P}(E,V) = \mathcal{W}(E,V) \frac{\exp[-\beta(E+PV)]}{\Omega}, \tag{9}$$

where $\mathcal{W}(E,V)$ is the number of microstates corresponding to an energy E and a volume V,

$$\mathcal{W}(E,V) = \sum_{(n)} \delta(V^{(n)} - V)\delta(H^{(n)} - E), \tag{10}$$

and is linked to the microcanonical entropy by $\mathcal{W}(E,V) = \exp S(E,V)$.

Using Eq. (9), microcanonical events at constant pressure are obtained by sorting the canonical distribution,

$$P_{\beta,P}^{(n)} = \frac{\exp[-\beta(H^{(n)} + PV^{(n)})]}{\Omega}, \tag{11}$$

according to the total energy $E=H^{(n)}$ [30]. The microcanonical phase diagram can also be exactly calculated from the sampling of the canonical distribution [Eq. (11)] [22,30], as it will be explained in greater detail in Sec. IV.

Numerics and convergence

To numerically sample the canonical partition sum (7) and access microcanonical thermodynamics through Eq. (9), we first recall that the canonical partition sum of a classical system can be factorized into its kinetic and potential components depending separately on the momentum and configuration space, respectively,

$$\Omega = \Omega_{kin}[\{\vec{p}_i\}]\Omega_{int}[\{\sigma_i\}].$$

Since Ω_{kin} is nothing but the partition sum of a classical monatomic gas, the lattice momentum distribution is simply given by a Maxwell-Boltzmann distribution which does not depend on the pressure P and is given by

$$f_{MB}(p_q) = (2\pi mT)^{-1/2} \exp\left(-\frac{p_q^2}{2mT}\right), \tag{12}$$

where p_q is the momentum component along the axis q $(=x,y,z)$ and $T=\beta^{-1}$ is the temperature. A three-dimensional momentum vector $\vec{p_q}$ is assigned to each cell to Eq. (12).

The average kinetic energy per particle in the canonical ensemble is always equal to $\langle E_{kin} \rangle = 3T/2$ and the corresponding fluctuation $\sigma^2 = 3T^2/2$; once partitions are sorted according to their total energy (microcanonical ensemble) this is not true any more. The distribution of the constant total-energy partitions deviate from Eq. (12) and abnormal kinetic-energy fluctuations appear at the crossing of first-order transition borders [30].

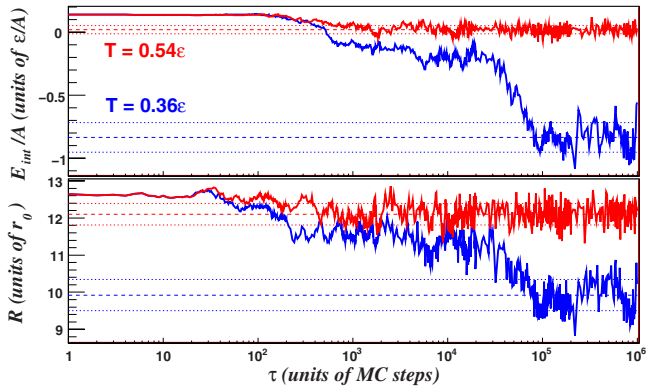

FIG. 1. (Color online) Evolution as a function of the Monte Carlo steps of the interaction energy per particle (upper part) and mean radius $R=\sqrt[3]{\langle R^3\rangle}$(lower part) for a system composed of 75 neutral and 54 charged particles at two different temperatures $T=0.36\epsilon$ (lower curve) and $T=0.54\epsilon$ (upper curve). Dashed lines: thermal average. Dotted lines: standard deviation. Calculations are done in the canonical ensemble.

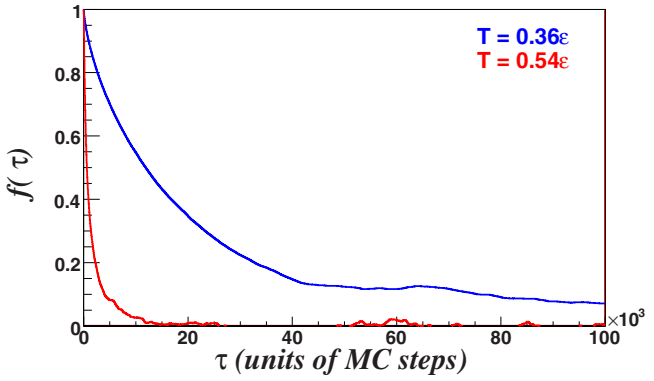

FIG. 2. (Color online) Autocorrelation function [Eq. (14)] as a function of the sampling period for a system composed of 75 neutral and 54 charged particles at two different temperatures $T=0.36\epsilon$ (upper curve) and $T=0.54\epsilon$ (lower curve).

The configuration spin space $\{\sigma_i\}$ is numerically sampled for each given value of temperature and pressure with a standard Metropolis technique [17,31]. This algorithm is based on the detailed balance principle. Starting from an arbitrary configuration of site spins $\{\sigma_i\}$, we transform a configuration (1) into a configuration (2) by inverting the occupation of two randomly selected lattice sites. The probability of accepting the new configuration is given by

$$p^{(1)\to(2)} = \frac{P^{(1)}_{\beta,P}}{P^{(2)}_{\beta,P}} = \exp\{-\beta[H^{(1)}_{int} - H^{(2)}_{int} + P(V^{(1)} - V^{(2)})]\}. \quad (13)$$

This algorithm exactly preserves the total occupations, i.e., the total numbers of neutral particles, $N=\sum_{i=1}^{L^3}\delta(\sigma_i+1)$, and of charged particles, $Z=\sum_{i=1}^{L^3}\delta(\sigma_i-1)$.

Figure 1 gives the evolution of the canonical averages for the total interaction energy and radius, evaluated for a system composed of $A=129$ particles ($N=75$ neutral particles and $Z=54$ charged particles), at two different temperatures and a pressure $P=2.65\times10^{-5}\epsilon A/r_0^3$, as a function of the total number of Monte Carlo iterations. This particular number of particles is chosen because isotopically resolved nuclear multifragmentation data will be soon available on this system [32]. The chosen values of temperature and pressure are selected because they correspond to different regions in the phase diagram (see Sec. IV below).

Only the steady-state regime observed in Fig. 1, defined as the regime where average behaviors are independent of the chosen initial condition, is considered for the calculation of thermal averages. The transient regime linearly varies as a function of the temperature at a given pressure, with lower temperatures corresponding to longer transient Monte Carlo times. Typical values for the number of excluded initial iterations for our applications are on the order of $N_{trans}\approx10^5$. Such long transient times are imposed by the presence of a long-range interaction, which considerably slows down the numerical convergence with respect to standard lattice-gas calculations [17].

The chosen Metropolis algorithm [Eq. (13)], although optimizing the rejection rate, induces a strong correlation between successive configurations. To minimize possible bias, we calculate the autocorrelation function defined as

$$f(\tau) = \frac{1}{\sigma_{E_{int}}(T-\tau)}\int_0^{T-\tau} dt[H_{int}(t) - E_{int}][H_{int}(t+\tau) - E_{int}], \quad (14)$$

where $H_{int}(t)$ is the internal energy value $H^{(n)}_{int}$ of the configuration (n) obtained at Monte Carlo time t, τ is the time interval between two configurations, T is the total time of the sampling, and $\sigma_{E_{int}}(T-\tau)$ is the estimation of internal energy fluctuation calculated over the interval $T-\tau$.

This autocorrelation function is presented in Fig. 2 for a system composed of 54 charged and 75 neutral particles at two different temperatures. In the simulations presented in this paper, only one configuration out of N_{cor} accepted Metropolis moves is used for the computation of physical observables, where N_{cor} is fixed so as to have a negligible correlation, $f(\tau)\leq0.1$ (dashed line in Fig. 2). It is found that N_{cor} linearly increases with decreasing temperatures and increasing number of particles. For our applications, typical values are on the order of $N_{cor}\approx5\times10^4$. The last parameter to be fixed to define the numerics is the total number of configurations, N_{ev}, which is used to compute the physical observables.

We have chosen three observables corresponding to three levels of description demanding different precisions, namely, the average canonical potential energy E_{int}, its fluctuation $\sigma_{E_{int}}$, and its probability distribution $P_{\beta,P}(E_{int})$. These observables are compared in Fig. 3 to the corresponding values obtained with a number $N^{\infty}_{ev}=2\times10^6$ of sampled configurations [33], which are indicated with an exponent ∞ in Fig. 3. These calculations have been done for a system with 75 neutral and 54 charged particles, at a temperature $T=0.36\epsilon$ and a pressure $P=2.65\times10^{-5}\epsilon A/r_0^3$. In these conditions the system is in an ordered liquidlike phase (see Sec. IV).

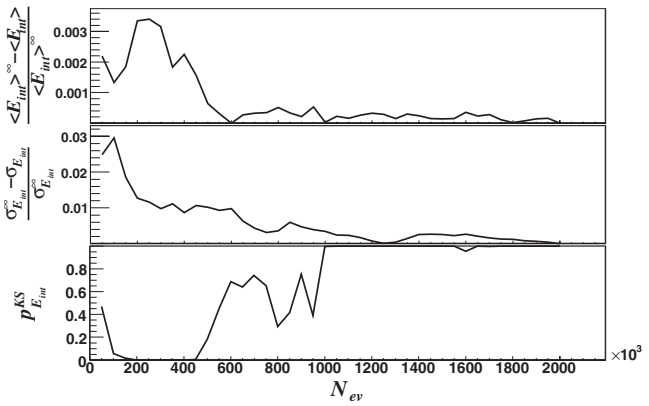

FIG. 3. Convergence of the Metropolis algorithm for a system composed of 75 neutral and 54 charged particles at the temperature $T=0.36\epsilon$. As a function of the number of recorded events N_{ev}, the upper (middle) part shows the relative difference of the average (standard deviation) of the interaction energy and its thermal value; the lower panel gives the Kolmogorov-Smirnov likelihood probability between the energy distribution with a given N_{ev} and its thermal limit.

Concerning the evolution of average observables (upper part of Fig. 3), we observe that $N_{ev} \approx 5 \times 10^4$ configurations are enough to ensure a deviation between the asymptotic energy and its estimation with N_{ev} samplings less than 1%. To have the same precision on the estimation of a fluctuation (middle part of Fig. 3) a statistics ten times higher is needed, $N_{ev} \approx 5 \times 10^5$. Finally we will use the computation of distribution functions of observables to calculate the microcanonical phase diagram. To this purpose, we compare in the bottom part of Fig. 3 the Kolmogorov-Smirnov likelihood probability [34] between the energy distribution with a given N_{ev} and its thermal limit. To guarantee a correct reproduction of the probability distribution, a higher statistics $N_{ev}=10^6$ will be used.

III. GROUND-STATE PROPERTIES

As a first application of the model, we present in this section a study of the ground-state properties of finite systems as a function of the charged particle Z and neutral particle N numbers. Zero-temperature properties are not accessible to the Metropolis algorithm. To access ground-state configurations, we have employed the adaptative simulated annealing technique. To reach the absolute minimum of the potential energy, the method consists of a slow "cooling" of the system and a progressive "reheating" in the case of trapping in local minima.

A Monte Carlo time interval including $N_{ev}=k$ recorded configurations is used, which is divided into ten subperiods composed of k' steps. We note that $\langle H \rangle_i^{k'} = \frac{1}{k'} \sum_{j=kn+ik'}^{j=kn+(i+1)k'} H_{int}^{(j)}$ is the average potential energy obtained within the ith subperiod, while $\langle H \rangle_n^k = \frac{1}{10} \sum_{i=0}^{i=9} \langle H \rangle_i^{k'}$ is the average potential energy computed in the nth period.

The Monte Carlo "temperature" associated with the period $n+1$ is calculated as

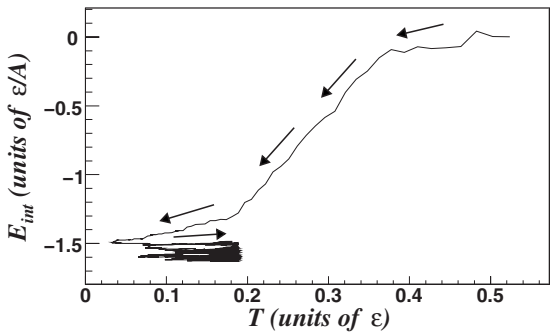

FIG. 4. Correlation between the interaction energy and the Metropolis temperature in the adaptative simulated annealing technique, for a system composed of 75 neutral and 54 charged particles.

$$T_{n+1} = \begin{cases} \dfrac{1}{a_n} T_n & \text{if} \quad \sharp \{ \langle H \rangle_i^{k'} \leq \langle H \rangle_{n-1}^{k} \} = 0, \qquad a_{n+1} = a_n^{1/r} \\ a_n T_n & \text{if} \quad \sharp \{ \langle H \rangle_i^{k'} \leq \langle H \rangle_{n-1}^{k} \} \in [1,4], \quad a_{n+1} = a_n \\ a_n T_n & \text{if} \quad \sharp \{ \langle H \rangle_i^{k'} \leq \langle H \rangle_{n-1}^{k} \} \geq 5, \qquad a_{n+1} = a_n^{r}, \end{cases} \tag{15}$$

where $r=0.9$, $a_n \in]0.96, 0.996[$ [35], and #{test} is the number of successful verifications of the test. The fictitious temperature defined by Eq. (15) is then used in the usual Metropolis algorithm [Eq. (13)].

The evolution of the average canonical interaction energy and fictitious temperature for the simulated annealing algorithm is presented in Fig. 4 for a representative case. We can observe at first a reduction in the temperature leading to a reduction in the energy up to saturation; this value corresponds to a local minimum in the potential-energy surface; successive oscillations in the temperature allow us to explore neighboring configurations and finally converge to the absolute interaction energy minimum.

The short-range part of the ground-state interaction energy E_{nuc} is shown in Fig. 5 as a function of the number of particles for an isospin symmetric system $N=Z$ (left side)

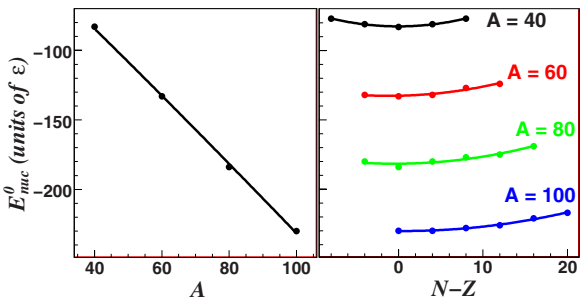

FIG. 5. (Color online) Left: average ground-state energy associated with the short-range coupling part of the Hamiltonian as a function of the number of particles for a symmetric $N=Z$ system. Right: same as left, as a function of the asymmetry between charged and neutral particles, for different total number of particles: $A=40,60,80,100$ from top to bottom. The lines correspond to best fits using Eq. (16).

TABLE I. Value of the different parameters appearing in the ground-state functional (16). "isoLGM" indicates the best fit of the Lattice-gas ground states, while "LDM" (liquid drop model) gives the standard nuclear physics result from the fit of nuclear masses [36].

	a_v^0	a_s^0	c_{sym}^0	α_c	r_0
isoLGM	−15.9 MeV	14.8 MeV	20.4 MeV	0.554 MeV fm	1.17 fm
LDM	−15.68 MeV	18.56 MeV	28.1 MeV	0.717 MeV fm	1.25 fm

and as a function of the isospin asymmetry for four different selected numbers of particles (right side). The full lines represent best fits using the liquid drop functional,

$$E_{nuc}^0(A,Z) = a_v^0 A + a_s^0 A^{1/3} + c_{sym}^0 \frac{(A-2Z)^2}{A}, \qquad (16)$$

where a_v^0, a_s^0, and c_{sym}^0 are fitting parameters. We can see that lattice-gas ground states, represented by the points in Fig. 5, are very well described by form (16), which gives an excellent representation of bulk properties of experimentally measured nuclear masses. If the coupling ϵ=5.5 MeV is used, which provides realistic nuclear saturation properties for infinite matter, the fitting parameters are also reasonably close to the physical volume, surface, and symmetry energy coefficients of atomic nuclei. The adequation between the value of the parameters and nuclear data is shown in Table I.

The long-range part of the ground-state interaction energy E_{coul} is shown in Fig. 6 for different numbers of particles and isospin asymmetries as a function of the square number of charged particles divided by the radius defined by Eq. (8) (right side). This last quantity is represented as a function of the number of particles in the left part of the same figure. Solid lines are fits with the functionals

$$E_{coul}^0(A,Z) = \alpha_c \frac{Z(Z-1)}{R}, \quad R = r_0 A^{1/3}. \qquad (17)$$

Some deviations are observed with respect to the expected Coulomb energy of uniformly charged spheres at a constant particle density. In particular we can see that, for a given particle number, the most charged system has the highest radius, meaning the saturation density decreases with increasing charge in a nonlinear way. A more sophisticated parametrization of the radius $R=r_0(A,Z)A^{1/3}$ would be needed to recover precisely the usual nuclear expression $E_{coul}^0=\alpha_c Z(Z-1)/(r_0 A^{1/3})$. However, Eq. (17) clearly gives a reasonably good description of the Coulomb energy and again the associated parameters α_c and r_0 are in good agreement with standard nuclear physics values (see Table I).

If nuclear shell and pairing corrections are obviously out of the scope of the present model, the gross adequation between lattice ground states and bulk properties of nuclear masses is remarkable. This means that the dominant part of nuclear masses can be explained in terms of generic statistical-mechanics models like the lattice gas. This is also encouraging for further applications of this same model at finite temperature where nuclear quantum effects, which are absent in the present description, are expected to be partially washed out.

The isoenergetic curves of lattice ground states are presented in Fig. 7. In this figure the total energy is evaluated as

$$E_{tot}^0(A,Z) = E_{nuc}^0(A,Z) + E_{coul}^0(A,Z), \qquad (18)$$

where the parameters of Eqs. (16) and (17) are the best-fit results given in Table I. Again the qualitative features of the stability line, defined as the lowest ridge of the total-energy hollow (thick line in Fig. 7), are similar to the physical case of nuclear masses. In the gray region of Fig. 7, the energies given by Eq. (18) do not correspond to stable lattice configu-

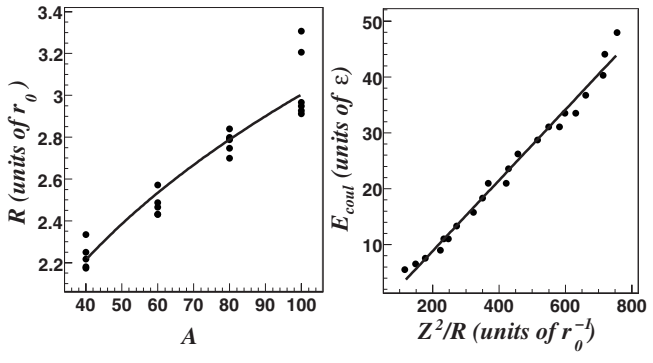

FIG. 6. Left: average ground state radius as a function of the total number of particles; the different points represent the different asymmetries shown in Fig. 5, the largest radius being associated to the highest total charge. Right: total Coulomb energy as a function of the square of the total charge divided by the average radius, for the same systems as in the left side. The lines correspond to best fits using Eqs. (17).

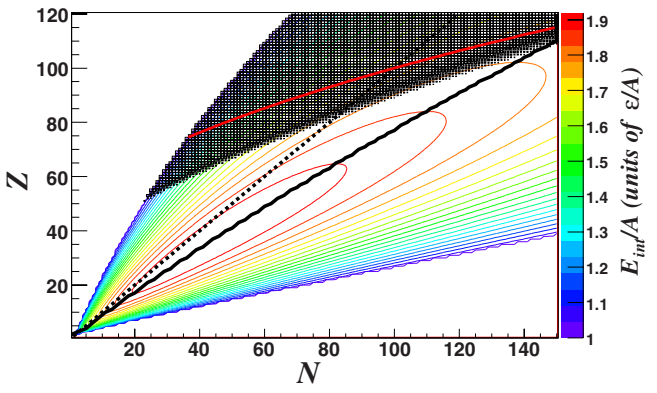

FIG. 7. (Color online) Contour lines: energy per particle extrapolated from the best fits according to Eq. (18), as a function of the number of neutral and charged particles. Full line: maximal stability line. Dotted line: $N=Z$. Dashed area: instability with respect to symmetric fission.

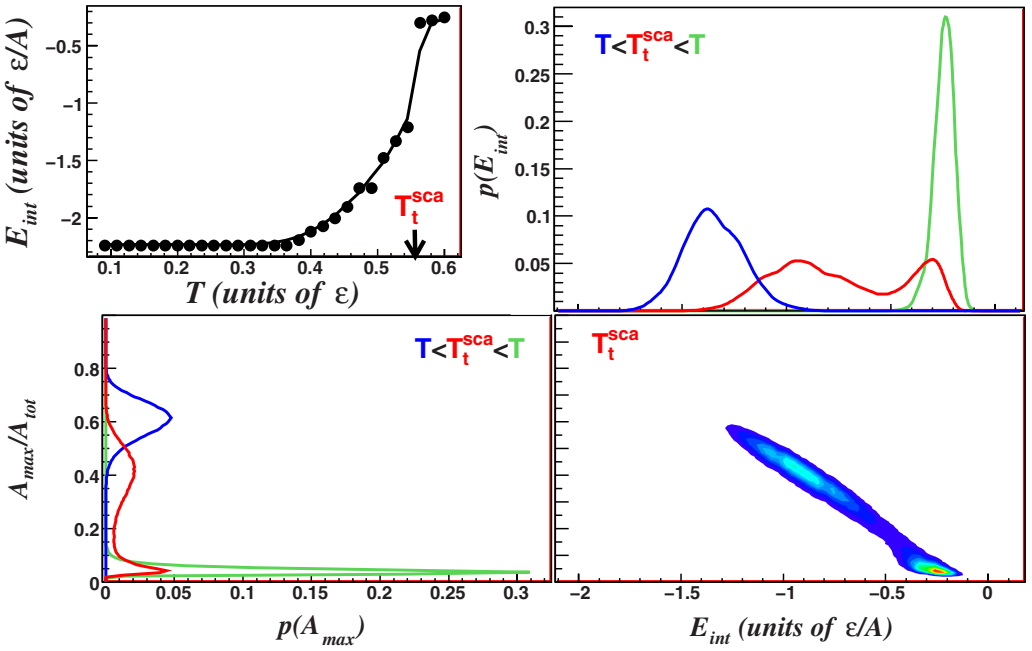

FIG. 8. (Color online) Thermal behavior of a system of 129 identical particles interacting with a short-range attractive force (standard LGM)at a pressure $P=2.65\times10^{-5}\epsilon A/r_0^3$. Upper left: average (full line) and most probable (symbols) interaction energies as functions of the temperature. The arrow gives the value of the transition temperature. Upper right: interaction energy distribution at a temperature below (dark gray), above (light gray), and at (black) the transition temperature. Lower left: distribution of the size of the largest cluster at a temperature below (dark gray), above (light gray), and at (black) the transition temperature. Lower right: correlation between the interaction energy and the size of the largest cluster at the transition temperature.

rations. Indeed the absolute minimum in this region found by the simulated annealing technique is a symmetric fission of the system into two separate clusters with a number of charged particles $Z_{max}=Z_{second}=Z/2$. The experimental fissility line is given by the dashed curve in Fig. 7. We can see again that the qualitative agreement is remarkable, especially considering that nuclear fission is a very complex, quantal, dynamical, and collective problem.

IV. PHASE DIAGRAM

We now turn to the determination of the finite-temperature phase diagram. Considering the similarity between the ground-state properties of the model and the energetics of atomic nuclei (see Sec. III), and the universality properties of phase transitions, we expect the lattice-gas phase diagram to be very close to that of nuclei. With only one type of particles, the lattice-gas model is well known to exhibit a first-order liquid-gas transition and a critical point (T_c, P_c) [16,22,30].

Adding a long-range repulsive Coulombic interaction, as well as a particle-type dependence of the short-range coupling, may deeply modify the characteristics of the phase diagram. In particular, the Coulomb interaction was shown to considerably affect the phase transition in different models. Not only the transition temperature has been reported to decrease with increasing Coulomb energy [18,37–39], but also the order and nature of the phase transition were observed to change [38,40]. It is therefore interesting to study the separate effect of the different components of the Hamiltonian on the lattice-gas model phase diagram.

First-order phase transitions in finite systems can be unambiguously defined from the convexity properties of the microcanonical entropy as a function of the order parameter [29,30]. In the case of transitions with finite latent heat, the total energy is an order parameter, and a first-order phase transition corresponds to negative microcanonical heat capacity $C_P^{-1}=-T_P^2 d^2 S_P/dE^2$. This latter can be computed from the canonical energy distribution according to

$$\frac{d^2 \ln p_{\beta,P}(E)}{dE^2} = -\frac{1}{C_P T_P^2} = -\frac{1}{T_P^2}\frac{dT_P}{dE}, \tag{19}$$

where T_P is the microcanonical temperature,

$$T_P^{-1} = \frac{dS_P}{dE}, \tag{20}$$

and the microcanonical entropy is given by

$$S_P(E) = \ln \int dV\, \mathcal{W}(E,V) \exp -\beta PV. \tag{21}$$

We start by presenting in Fig. 8 the evolution of a $A=129$-particle system at a constant pressure $P=2.65\times10^{-5}\epsilon A/r_0^3$ with a purely ferromagnetic isospin-independent interaction ($\epsilon_{11}=\epsilon_{-1-1}=\epsilon_{1-1}=\epsilon>0$) and without a Coulomb term.

The energy distributions at different canonical temperatures $T=\beta^{-1}$ are plotted in the upper right part of Fig. 8. The latter present a bimodal behavior over a narrow β interval where the microcanonical heat capacity is negative. The point where the two probability peaks have the same height

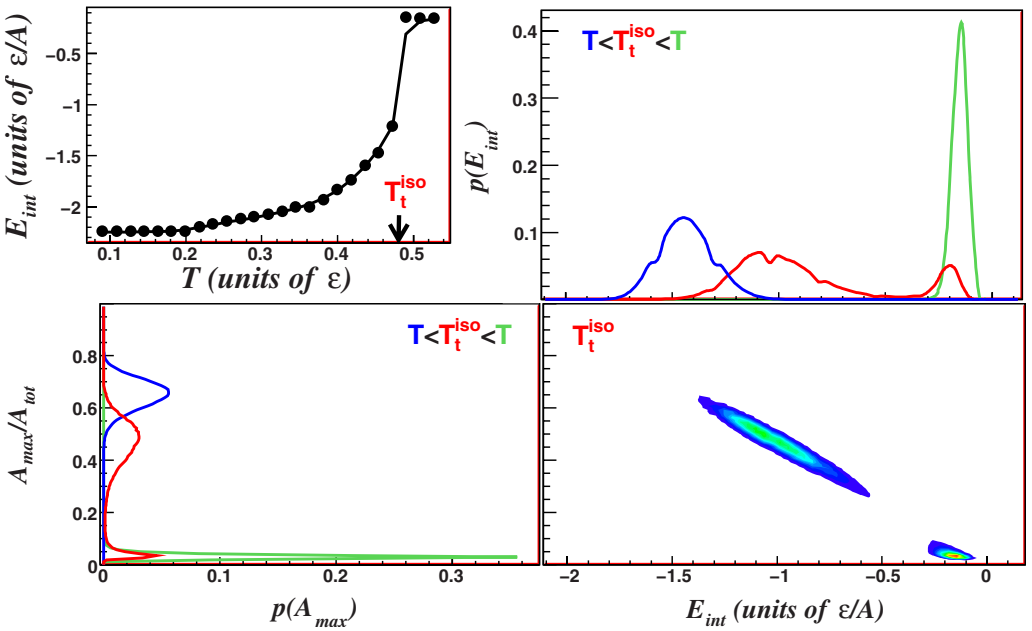

FIG. 9. (Color online) Thermal behavior of a system of 75 neutral and 54 charged particles interacting only with an isovector short-range force at a pressure $P=2.65\times10^{-5}\epsilon A/r_0^3$. Upper left: average (full line) and most probable (symbols) interaction energies as functions of the temperature. The arrow gives the value of the transition temperature. Upper right: interaction energy distribution at a temperature below (dark gray), above (light gray), and at (black) the transition temperature. Lower left: distribution of the size of the largest cluster at a temperature below (dark gray), above (light gray), and at (black) the transition temperature. Lower right: correlation between the interaction energy and the size of the largest cluster at the transition temperature.

is recognized as the first-order phase transition temperature T_t^{scalar} [41].

Due to the bimodality of the order parameter distribution, the most probable value of the potential energy in the canonical ensemble discontinuously jumps for $\beta^{-1}=T_t^{scalar}$ (symbols in the upper left part of Fig. 8). Conversely the average potential energy E_{int} defined in Eq. (3) varies continuously over the whole canonical temperature domain. Indeed the discontinuity in E_{int} associated with the presence of the latent heat would only be observable at the thermodynamic limit.

The lower left part of Fig. 8 presents the canonical probability distribution of the size of the largest cluster A_{max} present in each lattice configuration, at the same temperatures displayed for the energy distributions. This observable has been proposed to identify the fragmentation phase transition corresponding to the nuclear matter liquid-gas phase transition in heavy-ion collisions [42,43]. We can see that indeed this distribution is also bimodal, and that the transition temperature extracted from the bimodality of A_{max} remarkably coincides with the value extracted from the microcanonical heat capacity. The coincidence of the two estimations can be understood from the very strong linear correlation (lower right part of Fig. 8) between the interaction energy and the size of the heaviest cluster. This comforts the idea that A_{max}, which is experimentally a directly measurable observable, can be used as the order parameter of the fragmentation phase transition. Such a bimodality has been observed experimentally [44,45].

We now turn to examining the effect of a particle-dependent short-range coupling, considering $\epsilon_{11}=\epsilon_{-1-1}=0$, $\epsilon_{1-1}=\epsilon>0$. As discussed in the previous section, this isospin dependence of the interaction is responsible for the presence of the symmetry energy in nuclear physics. The choice of $\epsilon=5.5$ produces realistic results both in finite nuclei and infinite nuclear matter. The results, in the same conditions as in Fig. 8 above, are displayed in Fig. 9. We can see that the qualitative behavior is the same as for the standard isospin-independent lattice-gas model. The only difference concerns the value T_t^{iso} of the transition temperature, which is lower with respect to T_t^{scalar} at the same pressure value. This can be intuitively understood from the fact that the presence of an isospin-dependent interaction favors specific crystal-like configurations. On the other hand, the value of the latent heat (given by the energy jump in the upper left part of the figures, or the distance between the two maxima of the bimodal distribution in the upper right part) is almost unaffected by the short-range interaction. A much bigger difference between the numbers of charged and neutral particles than the one studied here ($N/Z=1.39$) would be needed to see an effect of the interaction on this observable [46]. Such exotic systems are not yet accessible experimentally.

In the previous calculations we had ignored the long-range repulsive Coulomb coupling. This frustrating interaction is expected to have a strong influence on the thermodynamics of the system [1,8,10,38,40,47], even if as in the nuclear case its energy contribution to the total binding can be considered as a perturbation since $I_c/\epsilon\approx0.26$.

Figure 10 is the same as Fig. 9 above, with the additional inclusion of the Coulomb coupling. We can see that the liquid-gas phase transition survives the presence of a Coulomb interaction, but the corresponding transition temperature T_t^{tot} is lowered. Moreover, the latent heat is considerably

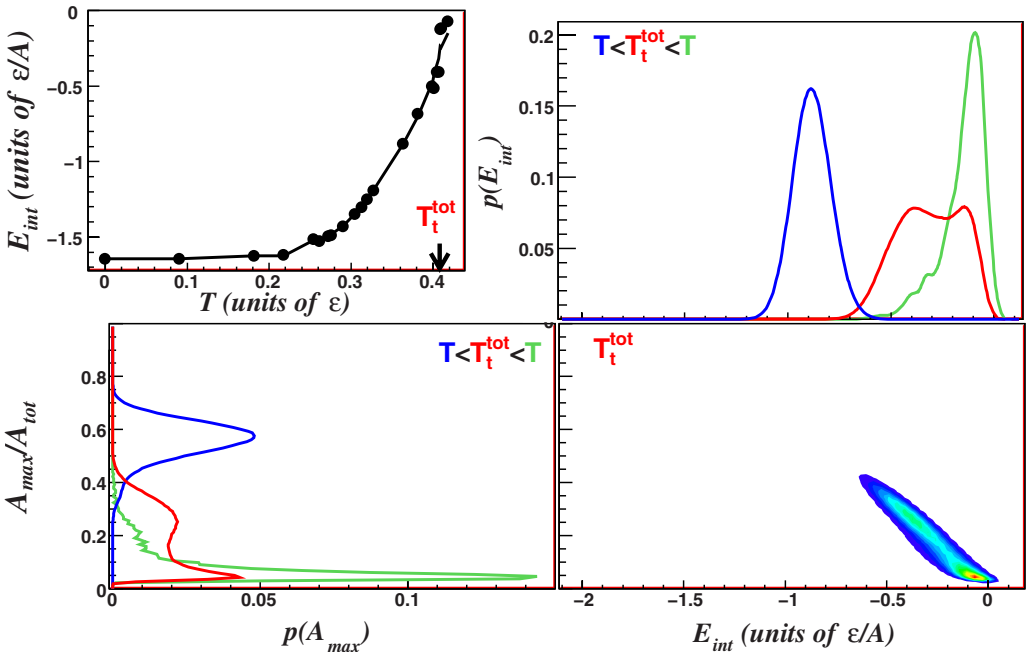

FIG. 10. (Color online) Thermal behavior of a system of 75 neutral and 54 charged particles interacting with an isovector short-range force and a repulsive long-range Coulombic force at a pressure $P=2.65\times10^{-5}\epsilon A/r_0^3$. Upper left: average (full line) and most probable (symbols) interaction energies as functions of the temperature. The arrow gives the value of the transition temperature. Upper right: interaction energy distribution at a temperature below (dark gray), above (light gray), and at (black) the transition temperature. Lower left: distribution of the size of the largest cluster at a temperature below (dark gray), above (light gray), and at (black) the transition temperature. Lower right: correlation between the interaction energy and the size of the largest cluster at the transition temperature.

reduced by the Coulomb interaction, in qualitative agreement with the results of realistic nuclear physics models [38]. The critical point is defined as the point in the (T,P) plane where the canonical bimodality disappears and the second derivative of the order parameter distribution probability vanishes [42], linked to the divergence of the microcanonical specific heat. The fact that the probability difference between the minimum and the maxima at the transition temperature is much smaller in Fig. 10 than in Figs. 8 and 9 shows that this last calculation is close to the critical point. The effect of the Coulomb force is thus to lower the critical point [37–40].

The evolution of the transition temperature with the different terms of the interaction is presented for two representative pressures in Table II. The reduction in the transition temperature due to the combined effect of Coulomb repulsion and isospin-dependent short-range forces is on the order of 25–30 %.

As discussed in Sec. III, the calculation of the canonical probability distributions demands a considerable numerical effort. The transition temperature can be alternatively recognized from the maximum of the order parameter fluctuation as it is shown in Fig. 11, which gives a precise and reliable measurement of the transition points and latent heat. In all cases, we observe a well-defined interaction energy fluctuation peak at the transition point. The calculation employing the complete isospin-dependent interaction produces, together with the energy fluctuation peak, two minor bumps at the temperatures T_a and T_b.

As observed for the probability distributions, estimations based on the size of the largest cluster (lower part of Fig. 11) precisely coincide with estimations using the interaction energy as an order parameter (upper part of Fig. 11). Moreover, A_{max} is a standard choice for an order parameter in a large class of fragmentation transitions [14]. If we consider A_{max} as an order parameter, we can see that the inflection points observed in the energy fluctuation curve with the complete interaction correspond to well-pronounced peaks of the A_{max} fluctuation.

These extra fluctuation peaks only appear if the repulsive long-range interaction and the particle-type dependence of the short-range force are simultaneously taken into account. This means that they mark transitions which are characteristic of the interplay between the Coulomb and symmetry energy, and do not correspond to any bulk matter limit. In the

TABLE II. Value of the liquid-gas transition temperature for a system composed of 75 neutral particles and 54 charged particles at two pressures $P=2.65\times10^{-5}\epsilon A/r_0^3$ (left column) and $P=1.06\times10^{-4}\epsilon A/r_0^3$ (right column) with different interactions: isospin-independent ferromagnetic closest neighbor coupling without (H_{scalar}) and with ($H_{scalar+coul}$) inclusion of a long-range repulsive Coulomb coupling among charged particles; isospin-dependent coupling without (H_{iso}) and with (H_{tot}) Coulomb interaction. The frustration strength has been fixed to $I_c/\epsilon=0.26$ to simulate nuclear systems.

	$P=2.65\times10^{-5}A\epsilon r_0^{-3}$	$P=1.06\times10^{-4}A\epsilon r_0^{-3}$
H_{scalar}	0.56ϵ	0.67ϵ
$H_{scalar+coul}$	0.51ϵ	0.62ϵ
H_{iso}	0.49ϵ	0.58ϵ
H_{tot}	0.41ϵ	0.49ϵ

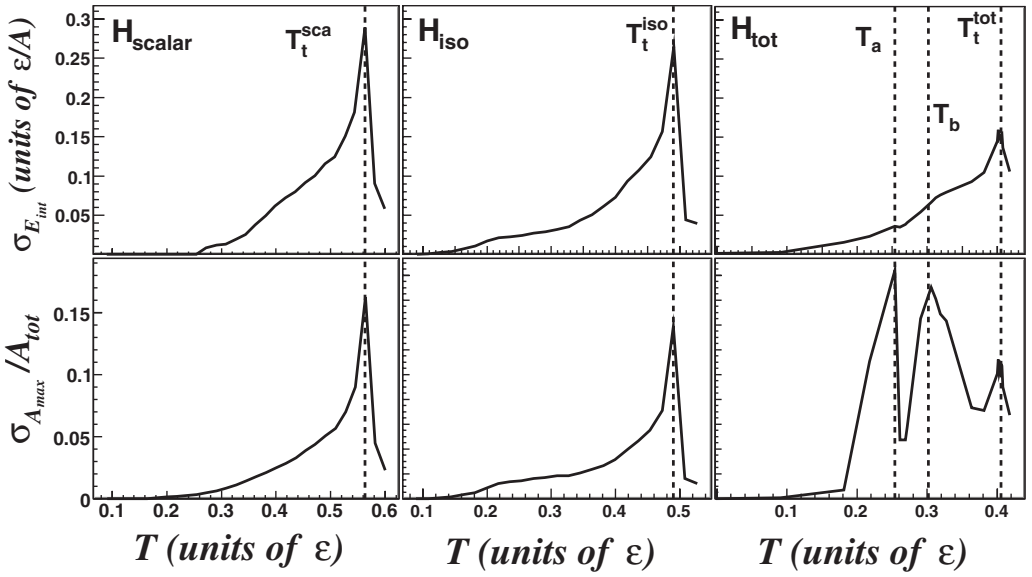

FIG. 11. Fluctuations of the interaction energy (upper panels) and of the size of the largest cluster (lower panels) versus temperature. Left side: same conditions as in Fig. 8; middle: same conditions as in Fig. 9; right side: same conditions as in Fig. 10. The dashed lines indicate the fluctuation peak.

following, we analyze in greater detail these extra fluctuation peaks to tentatively associate them with the specific nuclear physics phenomenology.

Fission-evaporation transition

To better understand the origin of the A_{max} fluctuation peaks which do not appear as interaction energy fluctuation maxima, we have plotted in the left part of Fig. 12 the correlation between the interaction energy and the size of the largest cluster at the three temperatures of interest, T_a, T_b, and T_t^{LG}. We can clearly distinguish the liquid-gas transition (bottom panels in Fig. 12) from the two others: only at the liquid-gas transition point the interaction energy distribution is bimodal, reflecting a finite latent heat.

At the other transition points T_a and T_b, the size of the largest cluster follows a bimodal distribution, while the two phases are characterized by very close interaction energies. We can therefore identify the points T_a and T_b as two first-order transition points without any latent heat. This is similar to the first-order transition in the Ising model, where the magnetization change occurs without any energy jump. The

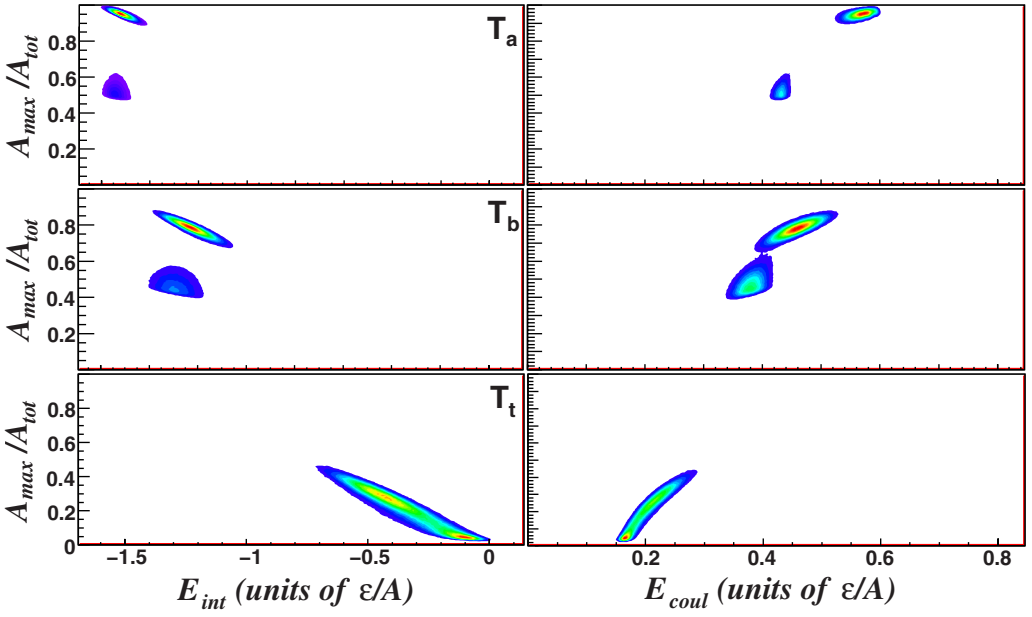

FIG. 12. (Color online) At the three transition temperatures defined by the right bottom panel in Fig. 10, the left part shows the correlation between the interaction energy and the size of the largest fragment; the right part shows the correlation between the Coulomb energy and the size of the largest fragment. Temperature increases from top to bottom. The conditions are the same as in Fig. 10.

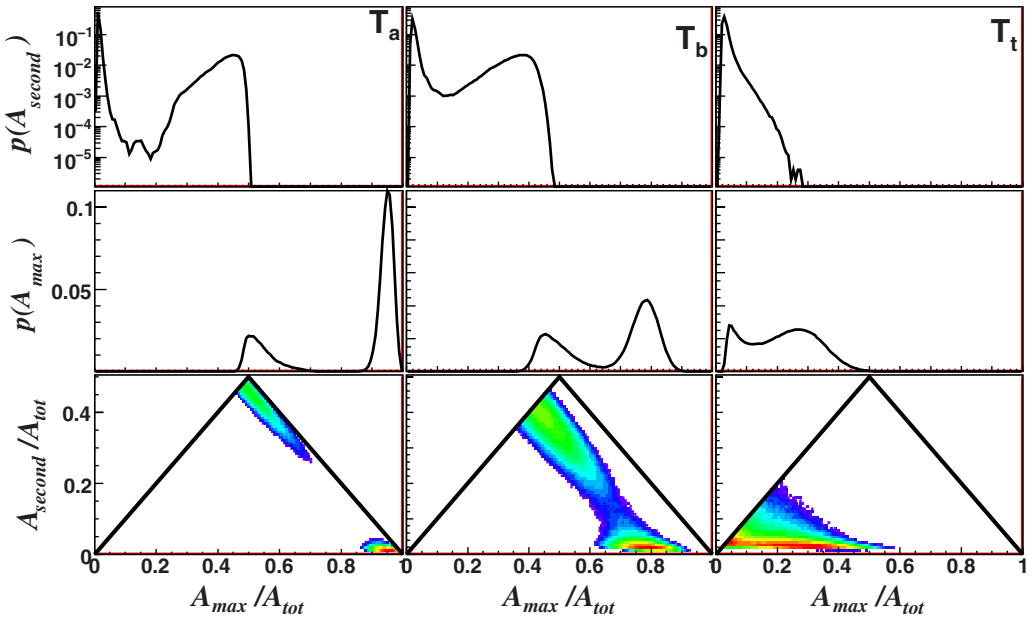

FIG. 13. (Color online) Distribution of the size of the largest (middle) and second largest (upper) clusters, and their correlation (bottom) at the three transition temperatures defined by the right bottom panel in Fig. 10. The conditions are the same as in Fig. 10.

right part of Fig. 12 shows that at this transition point the Coulomb energy distribution is bimodal. This means that the two coexisting phases at T_a and T_b correspond to similar total energies but very different Coulomb energies. This result is close to the findings of Refs. [38,40], where realistic fermionic densities of states are employed.

To better characterize this transition specific to the nuclear phenomenology, we show in Fig. 13 the distributions of the size of the two largest clusters A_{max} and A_{second}. At the transition points T_a and T_b, we observe either a dominant cluster (percolation cluster of the liquid-gas transition) followed by a very small second cluster ($A_{max} \gg A_{second}$), or two clusters of similar size ($A_{max} \sim A_{second}$). This transition point corresponds then to the coexistence between an evaporationlike phase and something close to symmetric fission. The trend is qualitatively the same at T_a and T_b, with an average size for the largest cluster decreasing with increasing temperature. This means that at the higher temperature the partitions include a large number of small clusters and monomers. We can also observe that the size of the second largest cluster is bimodal at these transition points, while only A_{max} is bimodal at the liquid-gas phase transition [11,15]. It is worth noting that several experimental analyses on heavy-ion-induced reactions around the Fermi energy have reported the observation of such bimodalities [44,45,48–50].

The complete phase diagram of the (N=75, Z=54) system can be computed by repeating the analysis presented in Figs. 8–10 at different values for the pressure P. At each pressure up to a limiting critical value, the total-energy distribution, as well as the distribution of the size of the heaviest cluster, presents two peaks of the same height at a temperature value, which is recognized as the liquid-gas transition temperature. If the pressure is below a limiting value P_{lim}, the distribution of A_{max} is additionally bimodal at two other temperature values. The ensemble of these transition points gives the transition lines, which are shown in Fig. 14.

The monotonically increasing line ending in a second-order critical point can be recognized as the liquid-gas phase transition. The qualitative phenomenology of this transition is not modified by the addition of a short-range isovector coupling and a long-range repulsive interaction. The main effect of Coulomb is to globally shift the transition line toward lower temperatures compared to the standard neutral lattice-gas model. In particular a bimodality is observed along this line in the total-energy distribution, showing that the liquid-gas transition has a finite latent heat also for finite charged systems.

But the phase diagram is considerably enriched with respect to liquid-gas. Two extra transitions appear at lower temperature which is specific to charged systems: inside the dashed curve, the system splits, without any energy jump, into two dominant fragments of similar size, which can be

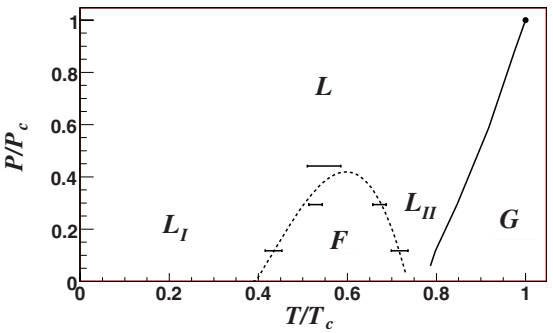

FIG. 14. (Color online) Phase diagram of a system of 75 neutral and 54 charged particles interacting with an isovector short-range force and a repulsive long-range Coulombic force at a pressure $P = 2.65 \times 10^{-5} \epsilon A / r_0^3$ (same conditions as in Fig. 10). The full line is the liquid (L)-gas (G) coexistence line and the point is the critical point. The symbols with horizontal error bars give fission (F)-residue (L) transition points. The dashed line is to guide the eye.

defined as hot fission. The two phases L_I and L_{II} observed on both sides of the fission phase correspond to partitions where the global system mass is dominated by a single cluster, which exhausts an important part of the mass in L_I, while it is accompanied by a large number of monomers and small fragments in L_{II}. Figure 14 shows that it is possible to continuously pass from L_I to L_{II}. Both phases can then be recognized as a representation of the liquid, in the same sense as liquid and gas are two different representations of a single fluid phase in ordinary liquid-gas. The findings in Fig. 14 clearly show that a bimodality is not only uniquely associated with the liquid-gas phase transition, but can also indicate other transitions that may or may not correspond to a bulk limit [51–53].

In particular the fission-liquid transition observed in the Coulombic Ising model with couplings optimized for nuclear physics is an effect of the competition in the small nuclear-like system between the attractive short-range coupling, which favors the persistence of a huge percolating cluster, and the repulsive long-range interaction, which favors binary splittings. This is a generic frustration phenomenon which may be encountered in different fields of physics, from magnets on specific lattices to liquid crystals, and from spin glasses to protein folding and neutron star crusts [1,4,6–10].

V. CONCLUSION

To conclude, we have presented in this paper a study of the phase diagram and fragment properties at zero and finite temperatures in the framework of a simple exactly solvable model, the lattice-gas model. A model interaction adapted to the description of atomic nuclei, including Coulomb and isospin-dependent terms, was considered. We still observed the existence of the liquid-gas transition with the addition of a long-range Coulomb interaction. As a surprising result, we have found at low temperature a phase transition triggered by the Coulomb energy, which corresponds to a fission-residue transition.

The relevance of the phase diagram calculated for this model to the nuclear physics phenomenology depends on how the fermionic nature of the system, completely ignored in this study, can modify the observed findings. In this respect it is interesting to observe that very similar results are obtained in phenomenological nuclear statistical models including realistic energy functionals and fermionic densities of states [38,40]. Concerning the possible experimental observation of this rich phenomenology, different multifragmentation data sets [44,45] have shown a clear bimodal feature for the distribution of the heaviest cluster.

A coarse comparison of the quasiprojectile fragmentation data of Ref. [45] and the distributions in Figs. 12 and 13 suggests that the fission-liquid transition may provide a better explanation of the data than the liquid-gas transition. It is however clear that a quantitative detailed comparison has to be done before a definitive conclusion can be reached, and the robustness of the predictions with respect to the employed modeling should be carefully analyzed.

[1] M. Grousson, G. Tarjus, and P. Viot, Phys. Rev. E **64**, 036109 (2001).
[2] T. D. Lee and C. N. Yang, Phys. Rev. **87**, 410 (1952).
[3] K. K. Mon and K. Binder, Phys. Rev. B **42**, 675 (1990).
[4] T. Müller and W. Selke, Eur. Phys. J. B **10**, 549 (1999).
[5] J. Lajzerowicz and J. Sivardiére, Phys. Rev. A **11**, 2079 (1975); **11**, 2090 (1975); J. Sivardiére and J. Lajzerowicz, *ibid.* **11**, 2101 (1975).
[6] S. Ray, J. Shamanna, and T. T. S. Kuo, Phys. Lett. B **392**, 7 (1997).
[7] A. B. MacIsaac, J. P. Whitehead, M. C. Robinson, and K. DeBell, Phys. Rev. B **51**, 16033 (1995); J. P. Whitehead, A. B. MacIsaac, and K. De'Bell, *ibid.* **77**, 174415 (2008).
[8] G. Tarjus, S. Kivelson, Z. Nussinov, and P. Viot, J. Phys.: Condens. Matter **17**, R1143 (2005).
[9] A. Sariban and K. Binder, J. Chem. Phys. **86**, 5859 (1987); J. A. Cuesta, L. Lafuente, and M. Schmidt, Phys. Rev. E **72**, 031405 (2005).
[10] P. Napolitani, Ph. Chomaz, F. Gulminelli, and K. H. O. Hasnaoui, Phys. Rev. Lett. **98**, 131102 (2007).
[11] F. Gulminelli, J. M. Carmona, P. Chomaz, J. Richert, S. Jimenez, and V. Regnard, Phys. Rev. E **68**, 026119 (2003).
[12] M. Pleimling and A. Hueller, J. Stat. Phys. **104**, 971 (2001).
[13] M. Kastner and M. Pleimling, Phys. Rev. Lett. **102**, 240604 (2009).
[14] J. M. Carmona, J. Richert, and P. Wagner, Phys. Lett. B **531**, 71 (2002).
[15] F. Gulminelli and Ph. Chomaz, Phys. Rev. C **71**, 054607 (2005).
[16] X. Campi and H. Krivine, Z. Phys. A: Hadrons Nucl. **344**, 81 (1992).
[17] J. Richert and P. Wagner, Phys. Rep. **350**, 1 (2001).
[18] C. B. Das *et al.*, Phys. Rep. **406**, 1 (2005).
[19] N. D. Cook, J. Phys. G **25**, 1213 (1999).
[20] Y. G. Ma *et al.*, Phys. Rev. C **69**, 064610 (2004).
[21] C. B. Das and S. Das Gupta, Nucl. Phys. A **812**, 149 (2008).
[22] F. Gulminelli, Ann. Phys. (Paris) **29**, 1 (2004).
[23] F. Gulminelli and G. Lehaut, Int. J. Mod. Phys. E **18**, 1022 (2009); G. Lehaut, F. Gulminelli, and O. Lopez, Phys. Rev. Lett. **102**, 142503 (2009).
[24] J. Pan and S. Das Gupta, Phys. Rev. C **57**, 1839 (1998).
[25] N. Sator, Phys. Rep. **376**, 1 (2003).
[26] C. Dorso and J. Randrup, Phys. Lett. B **301**, 328 (1993).
[27] Ph. Chomaz *et al.*, Ann. Phys. (N.Y.) **320**, 135 (2005).
[28] For a spherical homogeneous system, this definition of R exactly gives the expectation value of the average system cubic radius ($R^3=2\int_0^\infty r^3\rho dr^3/\int_0^\infty \rho dr^3$), while for other shapes it has to be interpreted as one of the different possible estimators of the spatial extension of a partition [27].
[29] D. H. E. Gross, *Microcanonical Thermodynamics: Phase Transitions in Small Systems*, Lecture Notes in Physics No. 66 (World Scientific, Singapore, 2001).

[30] F. Gulminelli and Ph. Chomaz, EPL **50**, 434 (2000); Ph. Chomaz, V. Duflot, and F. Gulminelli, Phys. Rev. Lett. **85**, 3587 (2000).
[31] N. Metropolis, J. Chem. Phys. **21**, 1087 (1953).
[32] G. Lehaut, Ph.D. thesis, LPC Caen, 2009; information is also available at http://indra.in2p3.fr
[33] Increasing N_{ev}^{∞} above this value does not modify the results.
[34] W. T. Eadie, D. Drijard, F. E. James, M. Roos, and B. Sadoulet, *Statistical Methods in Experimental Physics* (North-Holland, Amsterdam, 1971), pp. 269–271.
[35] G. Perrin, X. Descombes, and J. Zerubia, Proceedings of Energy Minimization Methods in Computer Vision and Pattern Recognition (EMMCVPR), St. Augustine, FL, USA, 2005 (unpublished).
[36] W. D. Myers and W. J. Swiatecki, Nucl. Phys. **81**, 1 (1966).
[37] M. J. Ison and C. O. Dorso, Phys. Rev. C **69**, 027001 (2004).
[38] F. Gulminelli, Ph. Chomaz, A. H. Raduta, and A. R. Raduta, Phys. Rev. Lett. **91**, 202701 (2003).
[39] P. Bonche *et al.*, Nucl. Phys. A **427**, 278 (1984).
[40] G. Chaudhuri, F. Gulminelli, and S. Das Gupta, Nucl. Phys. A **815**, 89 (2009).
[41] K. Binder and D. P. Landau, Phys. Rev. B **30**, 1477 (1984).
[42] Ph. Chomaz, F. Gulminelli, and V. Duflot, Phys. Rev. E **64**, 046114 (2001).
[43] F. Gulminelli, Nucl. Phys. A **791**, 165 (2007).
[44] M. Bruno *et al.*, Nucl. Phys. A **807**, 48 (2008).
[45] E. Bonnet *et al.*, Phys. Rev. Lett. **103**, 072701 (2009).
[46] C. Sfienti *et al.*, Phys. Rev. Lett. **102**, 152701 (2009).
[47] *Dynamics and Thermodynamics of Systems with Long Range Interactions: Theory and Experiments*, AIP Conf. Proc. No. 970, edited by A. Campa *et al.* (AIP, New York, 2007).
[48] N. Bellaize *et al.*, Nucl. Phys. A **709**, 367 (2002).
[49] P. Lautesse *et al.*, Phys. Rev. C **71**, 034602 (2005).
[50] M. Pichon *et al.*, Nucl. Phys. A **779**, 267 (2006).
[51] O. Lopez, D. Lacroix, and E. Vient, Phys. Rev. Lett. **95**, 242701 (2005).
[52] W. Trautmann, e-print arXiv:0705.0678.
[53] A. Le Fèvre and J. Aichelin, Phys. Rev. Lett. **100**, 042701 (2008).